



Article

Ant Colony Optimized Controller for Fast Direct Torque Control of Induction Motor

Hani Albalawi ^{1,2}, Sherif A. Zaid ^{1,*} , Mohamed E. El-Shimy ¹  and Ahmed M. Kassem ³¹ Electrical Engineering Department, Faculty of Engineering, University of Tabuk, Tabuk 47913, Saudi Arabia² Renewable Energy & Energy Efficiency Centre (REEEC), University of Tabuk, Tabuk 47913, Saudi Arabia³ Electrical Engineering Department, Faculty of Engineering, Sohag University, Sohag 82524, Egypt

* Correspondence: shfaraj@ut.edu.sa

Abstract: Induction motor (IM) drives have tremendous applications as high-performance drives in things such as mine winders, machine tools, electric vehicles, and elevators. Usually, IM drives controlled by direct torque control are preferred for these applications due to their fast torque control and simplicity compared with IM drives with field-oriented control. Proportional–integral–derivative (PID) controllers are commonly used to control IM drives using DTC. Though these controllers are simple and provide excellent response for linear systems with constant set points, they perform poorly with variable set points and IM motor parameter uncertainties. Hence, many control techniques and optimization algorithms have been applied to improve IM drive performance. This paper proposes an IM drive controlled using direct torque control principles, but with the power converter operation optimized to give fast torque performance. The IM drive speed response is improved using an optimized fuzzy PID (FPID). The FPID optimization is accomplished by the ant colony optimization (ACO) algorithm. All components of the IM drive with the optimized control system were simulated using the MATLAB/Simulink platform. The responses of the introduced drive using three different controllers—conventional PID, FPID, and optimized FPID—were compared. The simulation results indicate that the optimized FPID controller provided the best performance in terms of speed and torque. Additionally, the performance of the IM with the proposed optimized FPID under parameter uncertainties was studied. The simulation results indicated the robustness of the optimized FPID controller against parameter uncertainties.

Keywords: ant colony optimization (ACO); fuzzy PID; induction motor (IM); direct torque control (DTC)

check for updates

Citation: Albalawi, H.; Zaid, S.A.; El-Shimy, M.E.; Kassem, A.M. Ant Colony Optimized Controller for Fast Direct Torque Control of Induction Motor. *Sustainability* **2023**, *15*, 3740. <https://doi.org/10.3390/su15043740>

Academic Editor: Shuhua Fang

Received: 16 January 2023

Revised: 7 February 2023

Accepted: 14 February 2023

Published: 17 February 2023



Copyright: © 2023 by the authors. Licensee MDPI, Basel, Switzerland. This article is an open access article distributed under the terms and conditions of the Creative Commons Attribution (CC BY) license (<https://creativecommons.org/licenses/by/4.0/>).

1. Introduction

Recently, high-performance IM drives have been widely utilized in modern industrial applications such as mine winders, electric vehicles, elevators, and machine tools. Usually, high-performance drives are required to provide speed and accuracy, a wide speed control range, and a fast transient response [1–4]. These requirements of high-performance IM drives can be met by improving the torque response of the drive. The dynamic torque control of an IM can be achieved using two famous techniques: field orientation and DTC [5]. However, DTC has many advantages over field orientation, such as its simplicity, high accuracy, and fast torque response. In addition, the DTC procedure is considered to be robust against IM parameter uncertainties [6,7].

Traditional DTC has been implemented using hysteresis controllers, which cause a broad spectrum of inverter switching frequencies. This issue increases harmonics and complicates the filter design of the drive inverter [8]. Constantly sampled DTC has been proposed to alleviate the problems caused by hysteresis controllers in traditional DTC. A great deal of research on constant frequency DTC has been proposed [9–13]. However, the torque response in DTC has been considered in only a few studies [14,15].

In the literature, there are many proposed strategies and improvements that have recently been directed toward the torque response of IM drives that utilize DTC. The

principles of model predictive control (MPC) have been implemented in DTC-controlled IM drives [16,17]. The goal of MPC is to calculate the best inverter state to achieve the control objectives using a predefined cost function. The method has the advantages of low torque and flux ripples as well as high efficiency. However, it is complex, requires many calculations, and has reduced parameter uncertainty. Sliding-mode control has been introduced for DTC-controlled IM drives using feedback linearization in [18]. Though the controller was simple, it had high torque ripples and made a lot of noise. Ref. [19] has proposed an SVM-DTC algorithm using a super twisting sliding mode controller to improve drive performance. Ref. [20] has introduced and designed an optimal fuzzy controller for DTC-controlled IM drives. A hybrid control system including a fuzzy controller and a vector-control method has been developed for IMs in [21]. Ref. [22] has developed a model reference adaptive control that uses two speed estimators, one utilizing the back EMF and the other based on rotor flux. Adaptive neuro-fuzzy is one of the methods used for speed control in induction motors, e.g., in [23]. For induction motor drives and speed control, the brain emotional learning based on intelligent controller (BELBIC) has been developed [24]. Fuzzy and neural network techniques have been utilized for IM drives that use DTC [25–28]. Ref. [29] has proposed an implementation setup for a doubly fed IM controlled by DTC and optimized using ACO. The system, however, was complex and had to meet grid connection system standards. Ref. [30] introduces a new predictive DTC approach based on an optimized PWM. Although the idea is simple, the technique has been implemented mainly for permanent magnet synchronous motors.

Tuning of the proposed controller parameters can be accomplished using optimization techniques [31–33]. The results and system responses with these techniques were better than those achieved using conventional tuning methods. Nevertheless, these algorithms differ in terms of the complexity of the objective functions and the convergence speed. Presently, ACO, which is a metaheuristic optimization algorithm, is applied for many optimization problems [34]. Thanks to its simplicity and flexibility in implementation, the ACO algorithm has many power system applications [35]. In comparison with earlier efforts, the speed and torque responses of the proposed IM drive are improved using two cascaded optimizations. The first optimization stage is the speed response optimization using an FPID controller that has been optimized by the ACO technique. The second optimization stage is the optimization of the power converter operation to give fast torque performance. Furthermore, the responses of three different controllers (conventional PID, FPID, and optimized FPID) in conjunction with the introduced IM drive have been compared. The introduced drive has been tested using step and ramp speed disturbances. The IM drive response to model parameter uncertainties and variations in the IM parameters have also been studied.

This paper proposes an IM drive that utilizes direct torque control principles. The power converter operation has been optimized for high torque performance. On the other hand, the IM drive speed response is optimized using an optimized FPID. The FPID optimization is accomplished using the ACO algorithm. A constant sampling of the proposed drive has been implemented. All components of the IM drive with the optimized control system have been simulated using the MATLAB/Simulink platform. Comparisons of the responses of the introduced drive using three different controllers (conventional PID, FPID, and optimized FPID) have been carried out and the effects of the motor parameter variations on the optimization processes and drive performance have been studied.

The manuscript is prepared as follows. The IM modeling is described in Section 2. Section 3 explains the proposed DTC and optimum torque response of the IM. Section 4 explains the ACO algorithm. The design and optimization of the controller using ACO is described in Section 5. Section 6 discusses the results of the simulations. Finally, the research conclusions are presented in Section 7.

2. Induction Motor Model

To understand vector control in IM drives and to achieve perfect control aspects, a dynamic model of the IM is very important. The two-axis theory of machines provides excellent versions of the IM dynamic model based on the reference frame used. A suitable reference frame for the DTC of the IM is the stator reference frame [36]. By neglecting the slotting effects, iron losses, and air gap nonlinearities and assuming the infinite permeability of the iron parts, a dynamic model of the IM in the stator reference frame is given by [36]:

$$\begin{bmatrix} \bar{v}_s \\ \bar{v}_r \end{bmatrix} = \begin{bmatrix} r_s + pL_s & pL_m \\ (p - j\omega)L_m & r_r + (p - j\omega)L_r \end{bmatrix} \begin{bmatrix} \bar{i}_s \\ \bar{i}_r \end{bmatrix} \quad (1)$$

$$\begin{bmatrix} \bar{\lambda}_s \\ \bar{\lambda}_r \end{bmatrix} = \begin{bmatrix} L_s & L_m \\ L_m & L_r \end{bmatrix} \begin{bmatrix} \bar{i}_s \\ \bar{i}_r \end{bmatrix} \quad (2)$$

$$T = \frac{P}{3L_m} \cdot \text{Im} \{ \bar{\lambda}_s \bar{\lambda}_r^* \} \quad (3)$$

$$J_m \frac{d\omega}{dt} = T - T_l - \beta_v \omega \quad (4)$$

where (\bar{v}_r, \bar{v}_s) are the rotor and stator voltage vectors, respectively, $(\bar{i}_r$ and $\bar{i}_s)$ are the rotor and stator current vectors, respectively, $(\bar{\lambda}_s$ and $\bar{\lambda}_r)$ are the stator and rotor flux linkage vectors, respectively, $(L_m, L_r,$ and $L_s)$ are the mutual inductance, rotor, and stator inductances, respectively, (T) is the motor electromagnetic torque, (ω) is the motor speed, (β_v) is the viscous friction of the coupling, and (J_m) is the inertia of the IM rotor. Usually, the rotor windings are shorted in IMs. Hence, (\bar{v}_r) will be set to zero in Equation (1).

3. IM DTC and Optimal Torque Response

IM drives controlled by DTC have the merits of premium dynamic performance and simple implementation. These merits make them attractive for high-performance applications that demand accurate torque control. Usually, hysteresis controllers are utilized with conventional DTC. Unfortunately, hysteresis controllers select the voltage vectors in a manner that does not consider the optimum torque response of the IM [37]. Optimal torque or fast torque response may be realized by optimizing the inverter voltage vector. Hence, optimization will be adapted for the conventional DTC to achieve fast torque response. In the following paragraphs, the conventional DTC is reviewed, and the torque response is optimized.

3.1. DTC of IM

The three IM principles of conventional DTC are well documented in the literature [8]. According to these, both the IM torque and the stator flux are controlled independently. Torque control is achieved by regulating the angle between the rotor flux and the stator flux vectors. However, the stator flux is usually controlled to track its rated value. Regulation of the stator voltage vector selection has been the key to controlling both the torque and stator flux of the IM. The aim of DTC is to regulate both the torque and the flux inside a hysteresis band, as is shown in Figure 1. Hence, the rotation of the stator flux vector is regulated by the voltage vector selection. The traditional DTC rules for voltage vector selection are [10]:

1. Active voltage vectors rotate the stator flux vector, and, thereby, the flux and the torque will be decreased or increased.
2. Zero voltage vectors stop the motion of the stator flux vector, and, hence, the torque will be decreased and the flux will be fixed.
3. For each sector in the voltage vector plane, presented in Figure 1, there are two adjacent active voltage vectors that may be used to increase the torque. However, one increases the flux and the other decreases it. For instance, in sector (2), either vector V_2 or V_3 can be selected to increase the torque. On the other hand, V_3 decreases the stator flux, and V_2 increases the stator flux.

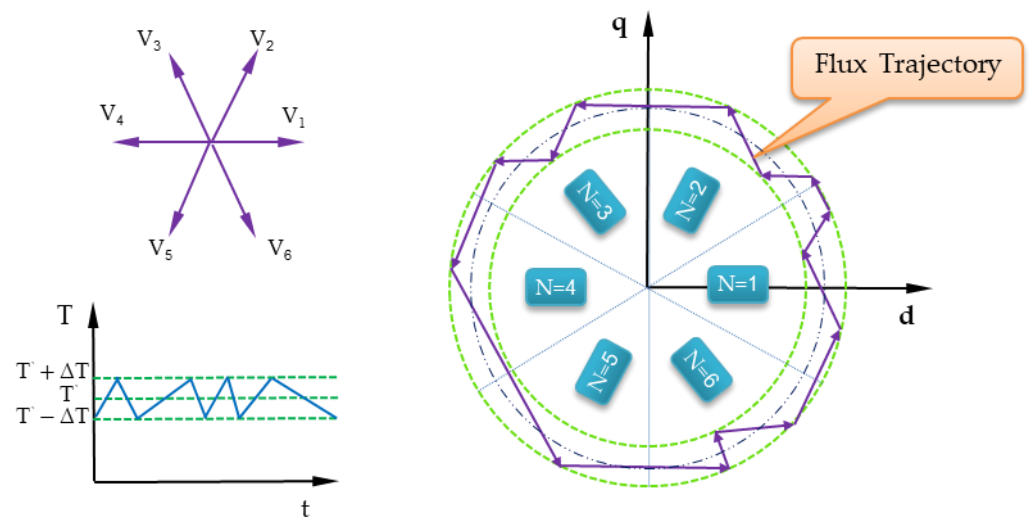


Figure 1. The typical torque and flux (trajectory) responses of 3-Φ IM with DTC.

Table 1 shows a summary of the DTC rules for selecting voltage vectors.

Table 1. The DTC rules used for selecting inverter states.

$\Delta\lambda$	ΔT	N					
		N = 1	N = 2	N = 3	N = 4	N = 5	N = 6
$\Delta\lambda = 1$	$\Delta T = 1$	V ₂	V ₃	V ₄	V ₅	V ₆	V ₁
	$\Delta T = 0$	V ₇	V ₀	V ₇	V ₀	V ₇	V ₀
$\Delta\lambda = 0$	$\Delta T = 1$	V ₃	V ₄	V ₅	V ₆	V ₁	V ₂
	$\Delta T = 0$	V ₀	V ₇	V ₀	V ₇	V ₀	V ₇

3.2. Optimization of the Inverter States for Maximum Torque Rate

The optimization approach must concentrate on choosing the voltage vector that delivers the greatest torque rate in order to achieve a quick torque response from the IM. The creation of the torque rate equation as a function of the stator voltage vectors is the initial stage in the optimization process. Hence, the relationship between the torque rate of the IM and the applied voltage vector must be derived. Differentiating the IM developed torque (2) with reference to time gives:

$$\frac{dT}{dt} = \frac{P}{3L_m} \cdot Im \left\{ \frac{d\bar{\lambda}_s}{dt} \bar{\lambda}_r^* + \bar{\lambda}_s \frac{d\bar{\lambda}_r^*}{dt} \right\} \tag{5}$$

It is assumed that the rotor flux vector has steady rotation and a constant peak during the stator flux variations. The reason behind this is the large rotor time constant of the IM [36]. Therefore, the rotor flux vector may be written as:

$$\bar{\lambda}_r = \lambda_r e^{-j(\omega t + \theta_{r0})} \tag{6}$$

where (λ_r) is the magnitude of the stator flux vector, (ω) is the rotor flux angular speed, and (θ_{r0}) is the initial rotor angle. Neglecting the stator resistance, the stator flux vector is related to the stator voltage vector by [8]:

$$\bar{\lambda}_s = V_n t + \bar{\lambda}_0 \tag{7}$$

where $(\bar{\lambda}_0)$ is the initial stator flux and (\bar{V}_n) is the inverter stator voltage vector of order (n) . Differentiating Equations (6) and (7) with reference to time, we obtain:

$$\begin{cases} \frac{d\bar{\lambda}_r^*}{dt} = -j\omega\bar{\lambda}_r^* \\ \frac{d\bar{\lambda}_s}{dt} = \mathbf{V}_n \end{cases} \quad (8)$$

Substituting Equations (6)–(8) into Equation (5) gives the following:

$$\frac{dT}{dt} = \frac{P}{3L_m} \cdot \text{Im} \left\{ (\mathbf{V}_n - j\omega(\mathbf{V}_n t + \bar{\lambda}_0)) \bar{\lambda}_r^* \right\} \quad (9)$$

If $t = 0$ (the time spent screening for the optimum state) and (9) is simplified, we obtain:

$$\frac{dT}{dt} = \frac{P}{3L_m} \lambda_r [V \sin(\theta_n - \theta_{ro}) - \omega \lambda_0 \cos(\theta_n - \theta_{ro})] \quad (10)$$

Let

$$\varphi = \tan^{-1} \left(\frac{\omega \lambda_0}{V} \right) \quad (11)$$

Hence, we obtain:

$$\frac{dT}{dt} = C \cdot \sin(\theta_n - \theta_{ro} - \varphi) \quad (12)$$

where (C) is constant.

For maximum torque rate, i.e., quick torque response, Equation (12) should be optimized for the available voltage vectors. The objective function (ξ) is:

$$\xi = \max_n [\sin(\theta_n - \theta_{ro} - \varphi)] \quad (13)$$

To perform the optimization process, an observer should be utilized to obtain the stator flux, the rotor flux, and the motor speed. Regrettably, the observer uses the IM parameters, which are regarded as uncertain. The effects of the uncertainty of the IM parameters on the proposed drive performance are considered in Section 6.

4. Ant Colony Optimization

ACO is a population-based metaheuristic approach which may be utilized to obtain reasonably good solutions to complex optimization problems [8]. Ant activation is coordinated through stimergy, which is an indirect communication method achieved by modifying the movement in their environment [38–43]. When ants move, they emit a trace of a chemical substance called a pheromone. When an isolated ant moving around randomly discovers a pheromone left by another ant, it may choose to follow that trace and strengthen it with its own pheromone. As more ants keep track of that trace, more pheromone is deposited, and the route becomes more attractive to future ants. The organizational process of an ant colony is considered an example of positive feedback. ACO is really driven by a group of software agents called “synthetic ants” which are looking for good solutions to a particular optimization problem.

ACO improves solution optimization by obtaining an updated pheromone trace and moving these ants in the search space according to mathematical formulas based on the transition probability and the total pheromone in the area. At every iteration, ACO produces global ants and computes their fitness. Updating is performed for pheromones and edges of weak areas. Local ants will be moved to better areas when fitness improves, or when a new random direction is determined. Updates are performed for ant pheromone and evaporated ant pheromone. Both local and global searches are utilized for continuous ACO.

The k th ant probability $P_k(i, j)$ is identified by the following equation:

$$P_k(i, j) = \begin{cases} \frac{[\tau(i, j)]^\alpha [\eta(i, j)]^\beta}{\sum_{(i, j) \notin Tabu_k} [\tau(i, j)]^\alpha [\eta(i, j)]^\beta} & \text{if } (i, j) \notin Tabu_k \\ 0 & \text{if } (i, j) \in Tabu_k \end{cases} \quad (14)$$

Equation (14) calculates the probability that the ant will move from the current state i to another state j , considering the following:

- The information about the problem is used to determine the attractiveness η of the move.
- The level of the move's pheromone is used to describe how the good move was used in the past.
- The $Tabu_k$ lists the forbidden moves.

The parameters α and β are utilized to calculate the relative influence of η versus τ . When iteration t is finished, all the ants have finished their solutions, and the pheromone levels are updated according to the following equation:

$$\tau(i, j) = \varphi \cdot \tau(i, j) + \Delta\tau(i, j) \quad (15)$$

where $\tau(i, j)$ is the amount of pheromone in a given state (i, j) , φ is a coefficient corresponding to the level of pheromone persistence, and $\Delta\tau(i, j)$ stands for the pheromone deposited in a given state (i, j) , typically given by:

$$\Delta\tau_{(i, j)}^k = \begin{cases} \frac{1}{L_k} & \text{if ant } k \text{ travels on state } (i, j) \\ 0 & \text{else} \end{cases} \quad (16)$$

where L_k is the cost of the k th ant's round (usually longer).

Figure 2 presents a flowchart for the ACO process.

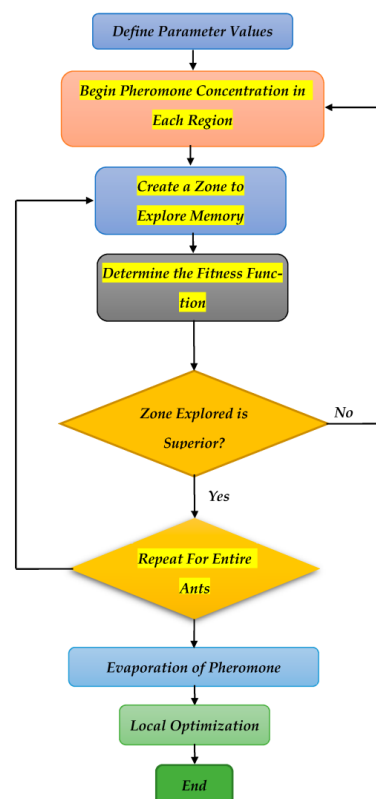


Figure 2. The ACO process flowchart.

The ACO operation sequence, shown in Figure 2, is as follows:

- Step 1: Set the ACO parameter values, such as α (parameter to control the influence of a pheromone trace), β (parameter to control the influence of a visibility value), number of iterations, and ρ (evaporation rate).
 - Step 2: Set the pheromone concentration (τ) for each region of ants.
 - Step 3: Generate the number of ants, place them at nodes that are selected probabilistically, and complete the tour as per the node selection.
 - Step 4: Evaluate the fitness function value.
 - Step 5: Check whether the region explored is better or not, update of region memory, and perform pheromone intensification.
 - Step 6: Repete the process for all the ants.
 - Step 7: Update the pheromone (evaporation and deposition) and generate new solutions.
 - Step 8: Check whether or not the stopping criterion (number of iterations) is achieved.
- End

5. Controller Design and Optimization

A block diagram of the introduced IM drive with the optimized controller is presented in Figure 3. Two optimizations are implemented inside the proposed system. The first or outer loop optimization is the speed controller parameter optimization. It utilizes the ACO algorithm to optimize the performance of the speed controller. However, the second optimization is implemented in the inner loop and optimizes the inverter states to achieve a fast torque performance according to Equation (13). The main controller is the speed controller that forms the outer loop in which the measured speed is compared with the commanded speed, producing the error that is considered the controller's input. The controller is an optimized FPID controller. The controller optimization is accomplished using the ACO algorithm. The output of the speed controller is the reference torque for the IM and represents the set point for the torque loop. It constitutes the inner loop in which another optimization process is adapted for fast torque response. The controller outputs the optimum voltage vector for the IM voltage source inverter. The control system will be described in the next section.

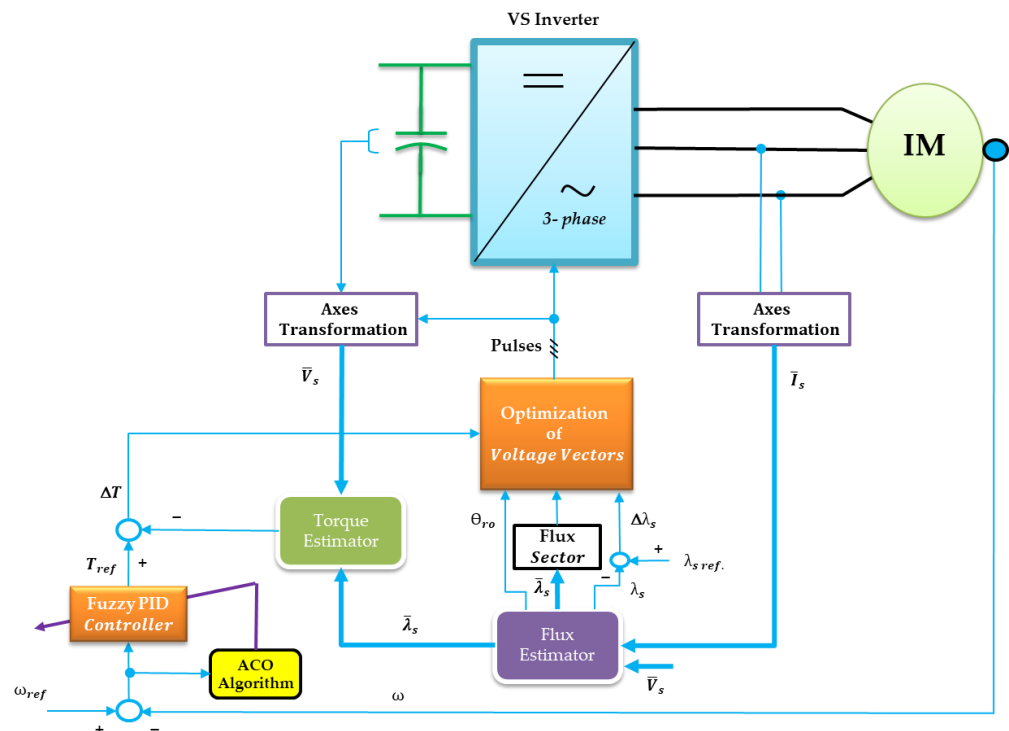


Figure 3. Block diagram of the proposed IM drive.

5.1. IM Control System

The proposed IM control system has digital controllers with a constant sampling period. Estimators for $(\bar{\lambda}_s, T, \text{ and } \theta_{r0})$ are implemented using the IM model equations and the measured currents and speed. The torque error (ΔT) and the estimated parameters are the inputs to the optimization algorithm of Figure 3. The optimization algorithm is as follows:

- If $\Delta T \geq 0$, then the optimum inverter state is (\bar{V}_0) .
- If $\Delta T < 0$, then the optimum inverter state is obtained based on the flux error ($\Delta \lambda$). The controller provides the inverter state as the traditional DTC if $|\Delta \lambda| > h$.
- If $|\Delta \lambda| \leq h$, then Equation (13) is used to select the optimum inverter state that provides the maximum rate of IM torque.

The outer loop is the speed controller loop. It has an optimized FPID controller that will be explained in the following section.

5.2. The Proposed FPID Controller

This controller is regarded as a fuzzy version of the conventional PID controller. Achieving fuzzy control of a system has four steps: fuzzification, rule base, fuzzy reasoning, and defuzzification. The fuzzification of the PID controller is accomplished using the same input signals as the traditional PID, but the controller is implemented with fuzzy rules.

The tuning of the FPID controller parameters is no longer an expert-based or pure knowledge process. Hence, it has the potential to be more convenient to execute. Reasoning and fuzzy rules are exploited here to produce the parameters of the controller. The parameters of the PID controller (K_p, K_i, K_d) are specified using the speed error $e(t)$ and error difference $\Delta e(t)$, where:

$$e(t) = r(t) - y_{out}(t) \quad (17)$$

$$\Delta e(t) = e(t) - e(t - \tau) \quad (18)$$

where τ is the sampling time.

5.2.1. Fuzzification of E and Δe

It is assumed that e and Δe have the specified ranges $[DK'_{p,\min}, DK'_{p,\max}]$, $[DK'_{i,\min}, DK'_{i,\max}]$ and $[DK'_{d,\min}, DK'_{d,\max}]$ respectively. It is suitable to normalize (e and Δe) by using the scaling factors K_e and K_{de} using the following linear transformation:

$$e_n(m) = K_e * e(m) \quad (19)$$

$$\Delta e_n(m) = K_{de} * \Delta e(m) \quad (20)$$

where K_e and K_{de} are the scaling factors for the fuzzy inputs (e and Δe).

The ambit of each linguistic value will be specified by a finer fuzzy partition with seven terms [44]. The linguistic values of the finer fuzzy partition are:

PS: Positive Small.

PM: Positive Medium.

PB: Positive Big.

Z: Zero.

NB: Negative Big.

NM: Negative Medium.

NS: Negative Small.

Each linguistic value is represented by a triangular membership function. The domain of each linguistic value determines the base of each triangle. The antecedent membership functions for e_n and Δe_n are presented in Figure 4.

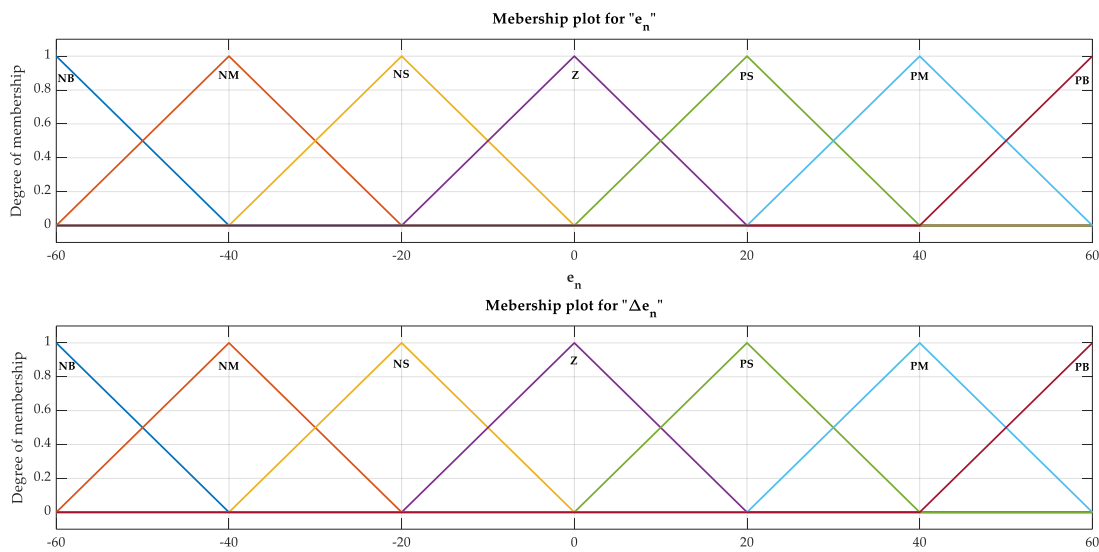


Figure 4. The membership functions for e_n and Δe_n .

5.2.2. Fuzzification of the Controller Parameters

It is assumed that DK'_p , DK'_i , and DK'_d are in the prescribed ranges $[DK'_{p,min}, DK'_{p,max}]$, $[DK'_{i,min}, DK'_{i,max}]$, and $[DK'_{d,min}, DK'_{d,max}]$, respectively, where DK'_p , DK'_i , and DK'_d are the outputs of a fuzzy control system.

In the proposed scheme, the PID parameters are set based on the current error $e_n(t)$ and its first difference $\Delta e_n(t)$. The resultant membership functions for DK'_p , DK'_i , and DK'_d are presented in Figure 5.

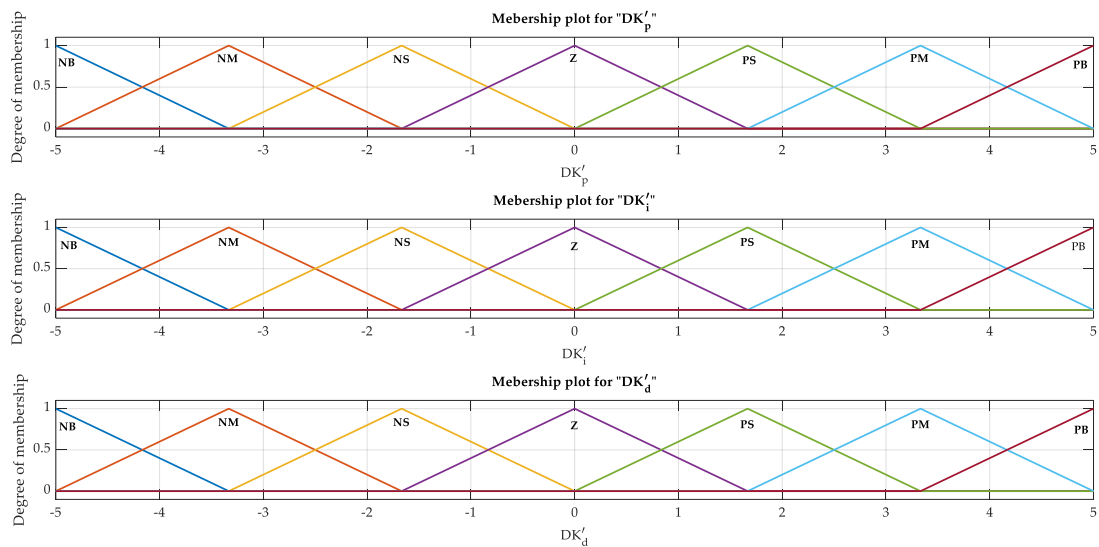


Figure 5. The membership functions for DK'_p , DK'_i , and DK'_d .

5.2.3. Rule Base, Fuzzy Reasoning, and Defuzzification

The fuzzy output parameters DK'_p , DK'_i , and DK'_d are assigned based on the following group of fuzzy rules:

If $e_n(i)$ is A_{1l} and $\Delta e_n(i)$ is A_{2l} , then DK'_p is B_{1l} , DK'_i is B_{2l} , and DK'_d is B_{3l} , where $\Delta e_n(i)$ is the i^{th} observation for normalized error-difference, $e_n(i)$ is the i^{th} observation for

normalized error, B_{1l} is a fuzzy set for output (1) and the l^{th} rule, A_{1l} is the fuzzy set for input (1) and the l^{th} rule, and l corresponds to 1, 2, 3, ... and is the rules order.

Tables 2–4 show the fuzzy output parameters rule base of (DK'_p , DK'_i , and DK'_d).

Table 2. Fuzzy tuning rules for DK'_p .

		$\Delta e_n(i)$						
		NB	NM	NS	ZE	PS	PM	PB
$e_n(i)$	NB	PB	PB	PM	PM	PS	Z	Z
	NM	PB	PB	PM	PS	PS	Z	NS
	NS	PM	PM	PM	PS	Z	NS	NS
	ZE	PM	PM	PS	Z	NS	NM	NM
	PS	PS	PS	Z	NS	NS	NM	NM
	PM	PS	Z	NS	NM	NM	NM	NB
	PB	Z	Z	NM	NM	NM	NB	NB

Table 3. Fuzzy tuning rules for DK'_i .

		$\Delta e_n(i)$						
		NB	NM	NS	ZE	PS	PM	PB
$e_n(i)$	NB	NB	NB	NM	NM	NS	Z	Z
	NM	NB	NB	NM	NS	Z	Z	NB
	NS	NB	NM	NS	NS	Z	PS	PS
	ZE	NM	NM	NS	Z	PS	PM	PM
	PS	NM	NS	Z	PS	PS	PM	PB
	PM	Z	Z	PS	PS	PM	PB	PB
	PB	Z	Z	PS	PM	PM	PB	PB

Table 4. Fuzzy tuning rules for DK'_d .

		$\Delta e_n(i)$						
		NB	NM	NS	ZE	PS	PM	PB
$e_n(i)$	NB	PS	NS	NB	NB	NB	NM	PS
	NM	PS	NS	NB	NM	NM	NS	Z
	NS	Z	NS	NM	NM	NS	NS	Z
	ZE	Z	NS	NS	NS	NS	NS	Z
	PS	Z	Z	Z	Z	Z	Z	Z
	PM	PB	NS	PS	PS	PS	PS	PB
	PB	PB	PM	PM	PM	PS	PS	PB

The t-norm is used to calculate the truth-value of the rule as the end connector to the antecedent part according to the following equation:

$$\mu_{A^l}(x) = \mu_{A_1^l}(x_{i1}) \otimes \mu_{A_2^l}(x_{i2}) \quad (21)$$

where $\mu_{A^l}(x)$ is the membership function resulting from the t-norm, x_{i1} is the i^{th} observation of entry number 1 and identical to $e_n(i)$, x_{i2} is the i^{th} observation for entry number 2 and

is identical to $\Delta e_n(i)$, A_1^l is the entry number 1 and the l^{th} rule of the fuzzy set, and A_2^l is the entry number 2 and the l^{th} rule of the fuzzy set.

Thus, when an engineering application agent is utilized, the membership function of the l^{th} fuzzy rule will be as follows:

$$\mu_{B^{l*}}(y) = \mu_{B^l}(y) \otimes [\mu_{A_1^l}(x_{i1}) \otimes \mu_{A_2^l}(x_{i2})] \quad (22)$$

Where y is the normalized output DK'_p , DK'_i , or DK'_d , $\mu_{B^l}(y)$ is the membership function for the specific output in the resultant and l^{th} rule, $\mu_{B^{l*}}(y)$ is the membership function resultant from the inclusion of the specific output in the resultant and l^{th} rule.

An output fuzzy set for every one of the rules is introduced by applying Equation (22) to every rule in the rule base. The generation of total output fuzzy set $\mu_Y(y)$ is determined by connecting these R fuzzy sets ($\mu_{B^{l*}}$). A t-conorm is used reasonably to connect the rules of the output fuzzy sets by yielding the union operator of the output fuzzy sets. The defuzzifier operation is used to interface the fuzzy output with the crisp domain.

δ_l is the center of gravity of the fuzzy set B^{l*} output of the l^{th} rule, and the output of the center of the defuzzifier area is given by the following equation:

$$y_{dn} = \frac{\sum_{l=1}^R \delta_l \mu_{B^{l*}}(\delta_l)}{\sum_{l=1}^R \mu_{B^{l*}}(\delta_l)} \quad (23)$$

where; y_{dn} is either DK'_p , DK'_i or DK'_d .

Thus, we can rewrite Equation (22) as follows:

$$y_{dn}(x_i) = y(x_{i1}, x_{i2}) = \frac{\sum_{l=1}^R \delta_l [\mu_{B^l}(\delta_l) \otimes \mu_{A_{jl}}(x_{ij})]}{\sum_{l=1}^R [\mu_{B^l}(\delta_l) \otimes \mu_{A_{jl}}(x_{ij})]} \quad (24)$$

The fuzzy set related to the j^{th} input variable and for the l^{th} rule is A_{jl} . The system inputs are partitioned into fuzzy sets that correspond to numeric indices (e.g., 1 to 7, respectively). The second index is l , whose values contain the set of numbers defining the partition of the input space. If the j^{th} input is partitioned into k_j membership functions where each one is specified by an integer between 1 and k_j , then the fuzzy set corresponding to the j^{th} input in the l^{th} rule should be $A_{jk(j,l)}$, where $k(j,l)$ is the function $k: \{1, 2\} \times \{1, 2, 3, \dots, R\} \rightarrow N$, where N is considered as a set of integer numbers. More precisely, $1 \leq k(j,l) \leq k_j$. Further, the notation can be made easily by denoting $\mu_{ij}(x)$ as the membership function for A_{ij} . The consequent part of the FLS will be determined by the same antecedent procedure. In this state, $h(l), h: \{1, 2, 3, \dots, R\} \rightarrow \{1, 2, \dots, H\}$ will be specified, where H is considered the number of membership functions assigned. The rule base is defined univocally by the functions $k(j,l)$ and $h(l)$. By this modification and more precise notation, Equation (24) will be:

$$y_{dn}(x_i) = y(x_{i1}, x_{i2}) = \frac{\sum_{l=1}^R \delta_{h(l)} [\mu_{B^{h(l)}}(\delta_{h(l)}) \otimes \mu_{A_{jk(j,l)}}(x_{ij})]}{\sum_{l=1}^R [\mu_{B^{h(l)}}(\delta_{h(l)}) \otimes \mu_{A_{jk(j,l)}}(x_{ij})]} \quad (25)$$

Equation (25) is a mathematical formula used to calculate the single numerical value obtained from the output of the fuzzy inference system.

If the values of DK'_p , DK'_i , and DK'_d are obtained, the parameters of the PID controller will be calculated from the following equations:

$$K_p = K_{p0} + K_{pf} * DK'_p \quad (26)$$

$$K_d = K_{d0} + K_{df} * DK'_d \quad (27)$$

$$K_i = K_{i0} + K_{if} * DK'_i \quad (28)$$

where K_{p0} , K_{d0} , and K_{i0} are the initial values of K_p , K_d , and K_i , respectively, and K_{p0} , K_{df} , and K_{if} are the scaling factors for fuzzy outputs DK_p , DK_i , and DK_{de} , respectively. The scaling factors K_{pf} , K_{df} , K_{if} , K_e , and K_{de} are optimized by the ant colony algorithm. The optimal parameters of the ACO controller are introduced in Table 5.

Table 5. Optimal ACO controller parameters.

Parameter	Value
No. of Ants	10
Max iterations	100
Number of parameters	5
Number of nodes for each parameter	1000
Evaporation rate	0.7

6. Results

The proposed IM drive system with the optimized controller, shown in Figure 3, is simulated using Matlab. The IM rating is (10 KW, 6 poles, 220 V, 60 Hz) and it has the parameters presented in Table 6.

Table 6. The proposed IM drive data.

Parameters			
$L_s = 0.0424$ H	$R_r = 0.156$ Ω	$L_r = 0.0417$ H	$J = 0.4$ kg·m ²
$L_m = 0.041$ H	$R_s = 0.294$ Ω	$\lambda_s = 0.454$ Wb	

Three controllers have been compared: the conventional PID, the FPID controller, and the ACO-optimized FPID controller. However, the internal optimization loop, used for the fast torque response, has been kept constant for the three controllers. The results were obtained under step and ramp variations in the set speed. In addition, there were load torque disturbances, as shown in Figure 6a,b. The IM speed responses with the three controllers are compared in Figure 6b. The ACO-optimized FPID controller clearly has the best speed response. It has the lowest settling time and steady-state error without overshooting. The worst response came with the classical PID controller. It has the largest settling time, overshoot, and steady-state error at all disturbances. The steady-state error value is not constant with the classical PID and FPID controllers; however, it varies with the disturbances. Additionally, it is observed that the step changes in the load torque at the times (1 s, 3 s, and 5 s) barely affect the IM speed with the proposed controller. On the other hand, these load torque disturbances produce small transients and slightly higher steady state errors with the classical PID and FPID controllers. Figure 6c shows profiles of the percentage speed errors for the three controllers. The ACO-optimized FPID controller has the lowest speed error profile.

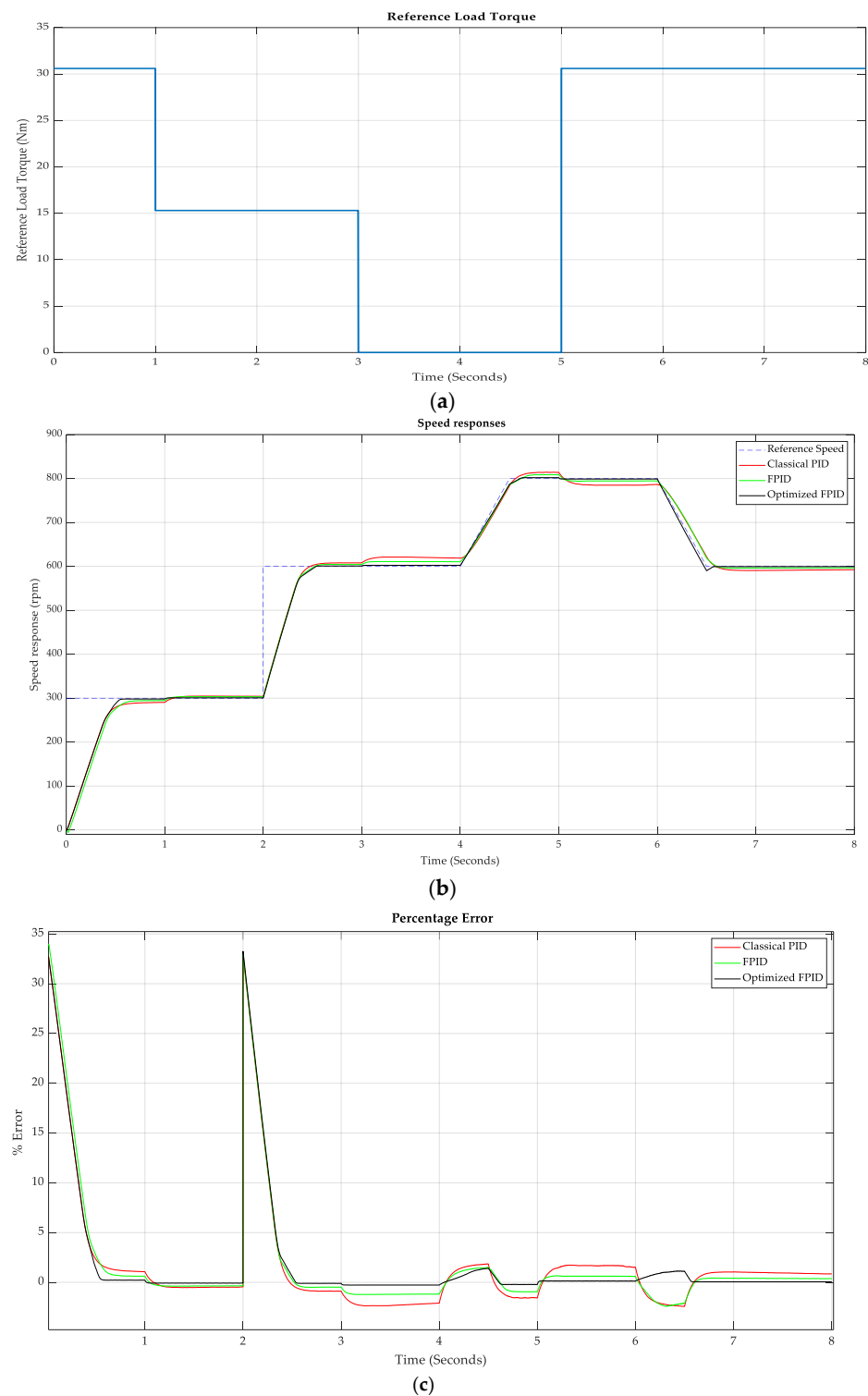


Figure 6. (a) Load torque profile, (b), comparison of the speed response of the IM drive, and (c) speed errors for three different controllers.

The torque and stator flux responses for the same set speed and load torque disturbances using the ACO-optimized FPID controller are presented in Figure 7. It is observed that the stator flux is kept constant at its rated value within a hysteresis band. This is important for the IM drive to possess its maximum torque in all circumstances. The profile of the IM torque compared with the commanded torque generated by the speed controller is also illustrated in Figure 7. During the transient periods corresponding to step changes

in the load torque, at the times (1 s, 3 s, and 5 s), the IM produces a torque that is greater than the load torque to accelerate the motor and reach the set speed. However, at steady state, the IM produces a torque equal to the load torque to keep the speed constant at the prescribed set value. During the ramp set speed interval, i.e., when the IM speed accelerates while the load torque is constant, the IM produces a torque that is greater than the load torque. The torque response of the IM is very fast and tracks the reference torque very well.

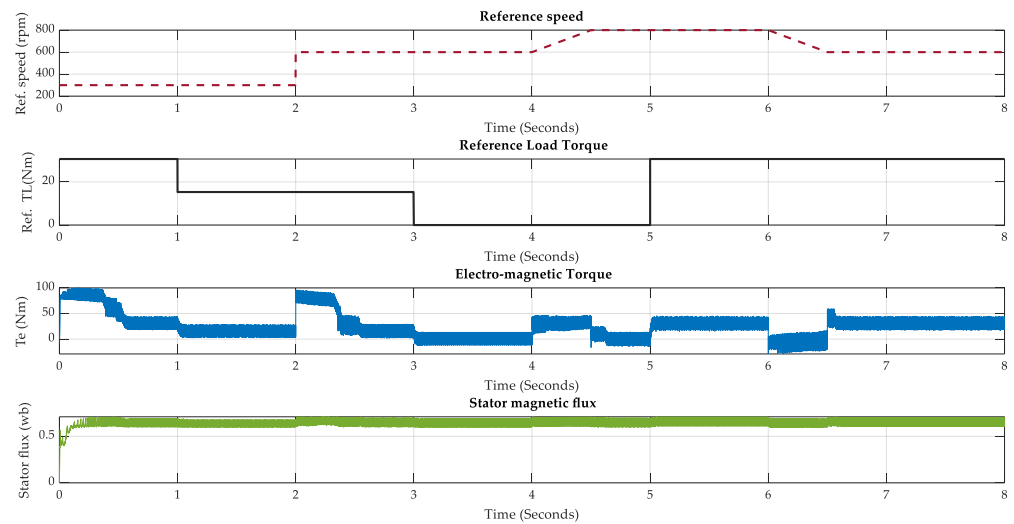


Figure 7. The optimized IM drive torque and stator flux responses.

The IM currents and phase voltage are shown in Figure 8. It has been indicated in the figure that the fundamental frequency of operation varies with IM speed. This is expected for DTC IM drives, which are equivalent to the voltage to frequency scalar control at steady state [8]. The stator direct and quadrature currents are AC, but their waveforms have some distortions in addition to the ideal sinusoidal waveforms. The reason behind this distortion is the high harmonic content of the inverter output voltage and the high complexity of the system. Because of the low impedance characteristics of the IM at low speeds, there is an initial inrush current when the IM motor starts.

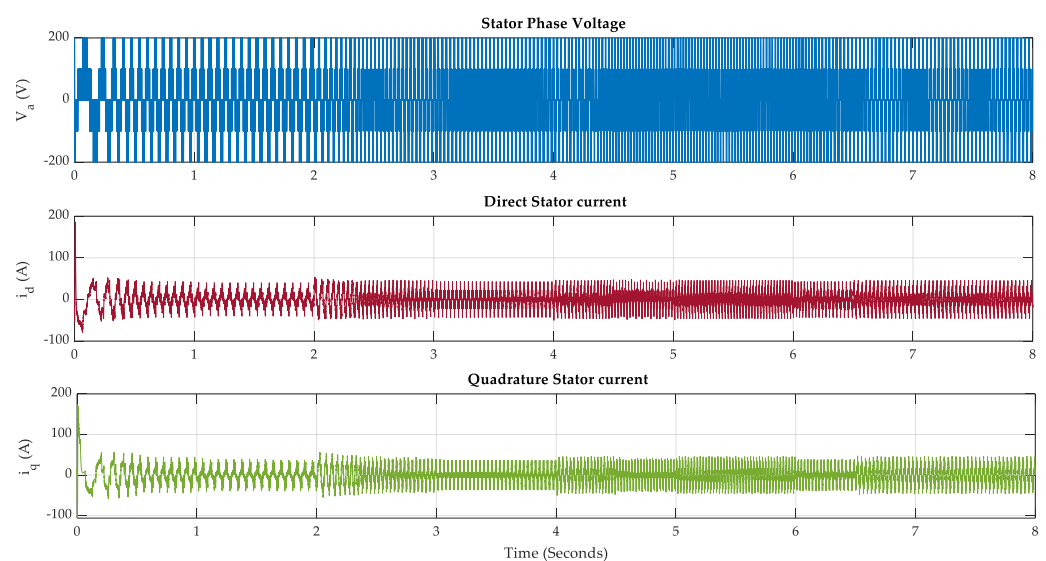


Figure 8. The optimized IM drive stator current and voltage responses.

To check the robust stability of the proposed ACO-optimized FPID controller against the IM parameter uncertainties, some of the IM variables are varied. The IM rotor resistance is increased by 10% and the IM rotor leakage reactance is increased by 5%. Figure 9

presents the speed response of the IM under parameter uncertainties. It is observed that the proposed controller can stabilize the speed response with high accuracy despite the modelling errors.

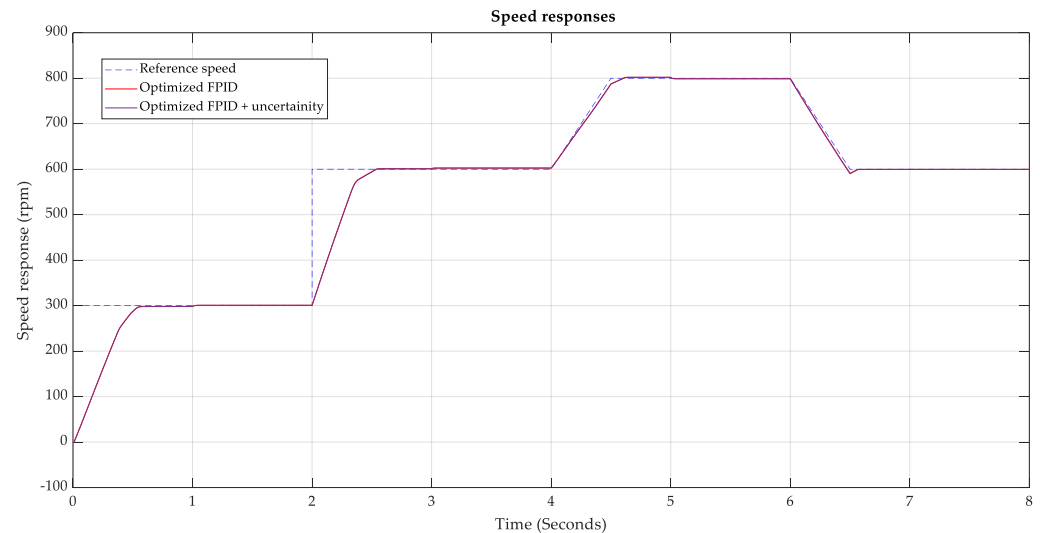


Figure 9. The speed response of the optimized IM drive under parameter uncertainties.

The percentage speed errors of the IM drive in the case of the three controllers have been listed in Table 7. The errors are determined using integral absolute error (IAE), integral square error (ISE), sum squared error (SSE), and time absolute error (TAE). It can be seen that the developed controller (the ACO-optimized FPID) is the best compared with the conventional and fuzzy PID controllers. In the case of the proposed controller, the percentage speed errors, e.g., the IAE, of the IM drive have dropped by about 4% and 7% compared with those of the FPID controller and the conventional PID, respectively.

Table 7. Comparison of the percentage speed errors for the three controllers.

	Conventional PID	FPID	ACO-Optimized FPID
%IAE	23.25	20.489	16.4
%ISE	2.963×10^3	3.135×10^3	2.89×10^3
%SSE	6.368	1.2176	0.0238
%TAE	54.88	38.436	23.28

7. Conclusions

This paper has proposed an IM drive controlled using direct torque control principles, but with the power converter operation optimized to give fast torque performance. Optimization analysis and design for the inverter operation were undertaken to achieve fast torque response. The IM drive speed response was improved by using optimized FPID. The FPID optimization was accomplished using the ACO algorithm. The proposed IM drive with the optimized control system was modelled and simulated using MATLAB/Simulink, and the responses of the introduced drive using three different controllers (conventional PID, FPID, and optimized FPID) were compared. The simulation results indicated that the optimized FPID controller provides the best speed and torque performances. In the case of the proposed controller, the percentage speed errors, e.g., IAE, of the IM drive dropped by about 4% and 7% compared with those of the FPID controller and the conventional PID, respectively. In addition, the IM performances under parameter uncertainties with the proposed optimized FPID were studied. The results indicated that under 10% variations in the rotor resistance and rotor leakage inductance, the system provides robust

performance. Future research relating to this topic will examine IM drive position control using the optimization methods adopted in this study. Moreover, the experimental validation of the proposed drive with the optimized FPID controller will be an important future consideration.

Author Contributions: Conceptualization, M.E.E.-S. and S.A.Z.; formal analysis, S.A.Z.; funding acquisition, A.M.K.; writing—original draft preparation, H.A.; writing—review and editing, H.A. All authors have read and agreed to the published version of the manuscript.

Funding: This research was funded by the University of Tabuk, grant number S-1442-0132.

Institutional Review Board Statement: Not applicable.

Informed Consent Statement: Not applicable.

Data Availability Statement: Not applicable.

Acknowledgments: The authors extend their appreciation to the Deanship of Scientific Research at the University of Tabuk for funding this work through grant number S-1442-00132.

Conflicts of Interest: The authors declare no conflict of interest.

References

1. Vas, P. *Sensorless Vector and Direct Torque Control*; Oxford University Press: New York, NY, USA, 1998.
2. Kazmierkowski, M.P.; Franquelo, L.G.; Rodriguez, J.; Perez, M.A.; Leon, J.I. High-Performance Motor Drive. *IEEE Ind. Electron. Mag.* **2011**, *27*, 6–26. [[CrossRef](#)]
3. Lascu, C.; Boldea, I.; Blaabjerg, F. A modified direct torque control for induction motor sensorless drive. *IEEE Trans. Ind. Appl.* **2000**, *36*, 122–130. [[CrossRef](#)]
4. Buja, G.S.; Kazmierkowski, M.P. Direct torque control of PWM inverter—Fed AC motors. *IEEE Trans. Ind. Electron.* **2004**, *51*, 744–757. [[CrossRef](#)]
5. Tiitinen, P.; Pohjalainen, P.; Lalu, J. The next generation motor control method DTC. *Rev. ABB* **1995**, *3*, 19–24.
6. Takahashi, I.; Noguchi, T. A New Quick Response and High-Efficiency Control Strategy of an Induction Motor. *IEEE Trans. Ind. Appl.* **1986**, *22*, 820–827. [[CrossRef](#)]
7. Alsofyani, I.M.; Bak, Y.; Lee, K. Fast Torque Control and Minimized Sector-Flux Droop for Constant Frequency Torque Controller based-DTC of Induction Machines. *IEEE Trans. Power Electron.* **2019**, *34*, 12141–12153. [[CrossRef](#)]
8. Zaid, S.A.; Mahgoub, O.A.; El-Metwally, K.A. Implementation of a New Fast Direct Torque Control Algorithm for Induction Motor Drives. *IET Electr. Power Appl.* **2010**, *4*, 305–313. [[CrossRef](#)]
9. Patil, U.V.; Suryawanshi, H.M.; Renge, M.M. Closed-loop hybrid direct torque control for medium voltage induction motor drive for performance improvement. *IET Power Electron.* **2014**, *7*, 31–40. [[CrossRef](#)]
10. Rosic, M.M.; Bebic, M.Z. Analysis of torque ripple reduction in induction motor DTC drive with multiple voltage vectors. *Adv. Electr. Comput. Eng.* **2015**, *15*, 105–114. [[CrossRef](#)]
11. Carmeli, M.S.; Mauri, M. Direct Torque Control as a variable Structure control: Existence Conditions Verification and Analysis. *Electr. Power Syst. Res.* **2011**, *81*, 1188–1196. [[CrossRef](#)]
12. Zhang, Z.; Tang, R.; Bai, B.; Xie, D. Novel Direct Torque Control Based on Space Vector Modulation With Adaptive Stator Flux Observer for Induction Motors. *IEEE Trans. Magn.* **2010**, *46*, 3133–3136. [[CrossRef](#)]
13. Shyu, K.-K.; Lin, J.-K.; Pham, V.-T.; Yang, M.-J.; Wang, T.-W. Global Minimum Torque Ripple Design For Direct Torque Control Of Induction Motor Drives. *IEEE Trans. Ind. Electron.* **2010**, *57*, 3148–3156. [[CrossRef](#)]
14. Kumar, R.H.; Iqbal, A.; Lenin, N.C. Review of recent advancements of direct torque control in induction motor drives—A decade of progress. *IET Power Electron.* **2018**, *11*, 1–15. [[CrossRef](#)]
15. El-Shimy, M.E.; Zaid, S.A. Fuzzy PID Controller for Fast Direct Torque Control of Induction Motor Drives. *JES J. Electr. Syst.* **2016**, *12*, 687–700.
16. Habibullah, M.; Lu, D.D.C.; Xiao, D.; Rahman, M.F. A simplified finite-state predictive direct torque control for induction motor drive. *IEEE Trans. Ind. Electron.* **2016**, *63*, 3964–3975. [[CrossRef](#)]
17. Ouhrouche, M.; Errouissi, R.; Trzynadlowski, A.M.; Tehrani, K.A.; Benzaïoua, A. A novel predictive direct torque controller for induction motor drives. *IEEE Trans. Ind. Electron.* **2016**, *63*, 5221–5230. [[CrossRef](#)]
18. Lascu, C.; Jafarzadeh, S.; Fadali, M.S.; Blaabjerg, F. Direct Torque Control with Feedback Linearization for Induction Motor Drives. *IEEE Trans. Power Electron.* **2017**, *32*, 2072–2080. [[CrossRef](#)]
19. Ammar, A.; Benakcha, A.; Bourek, A. Closed-loop torque SVM-DTC based on robust super twisting speed controller for induction motor drive with efficiency optimization. *Int. J. Hydrogen Energy* **2017**, *42*, 17940–17952. [[CrossRef](#)]
20. Sudheer, H.; Kodad, S.F.; Sarvesh, B. Improvements in Direct Torque Control of Induction Motor for a Wide Range of Speed Operation Using Fuzzy Logic. *J. Electr. Syst. Inf. Technol.* **2018**, *accepted for publication*. [[CrossRef](#)]

21. Kumar, V.; Joshi, R.R. Hybrid Controller based Intelligent Speed Control of Induction Motor. *J. Theor. Appl. Inf. Technol.* **2007**, *3*, 71–75.
22. Meziane, S.; Toufouti, R.; Benalla, H. MRAS based Speed Control of sensorless Induction Motor Drives. *ICGST-ACSE J.* **2007**, *7*, 43–50.
23. Rashidi, F. Sensorless Speed Control of Induction Motor Derives Using Robust and Adaptive Neuro-Fuzzy Based Intelligent Controller. *IEEE Int. Conf. Ind. Technol. ICIT* **2004**, *2*, 617–627.
24. Abdollahi, R.; Farhangi, R.; Yarahmadi, A. Emotional Learning Based Intelligent Controllers for Rotor Flux Oriented Control of Induction Motor. *J. Electr. Eng.* **2014**, *65*, 228–234. [[CrossRef](#)]
25. Pimkumwong, N.; Wang, M.-S. Online Speed Estimation Using Artificial Neural Network for Speed Sensorless Direct Torque Control of Induction Motor Based on Constant V/F Control Technique. *Energies* **2018**, *11*, 2176. [[CrossRef](#)]
26. Sung, G.-M.; Wang, W.-Y.; Lin, W.-S.; Yu, C.-P. Predictive Direct Torque Control Application-Specific Integrated Circuit of an Induction Motor Drive with a Fuzzy Controller. *J. Low Power Electron. Appl.* **2017**, *7*, 15. [[CrossRef](#)]
27. Abbasi Moshaii, A.; Mohammadi Moghaddam, M.; Dehghan Niestanak, V. Fuzzy sliding mode control of a wearable rehabilitation robot for wrist and finger. *Ind. Robot.* **2019**, *46*, 839–850. [[CrossRef](#)]
28. Abbasimoshaei, A.; Mohammadimoghaddam, M.; Kern, T.A. Adaptive fuzzy sliding mode controller design for a new hand rehabilitation robot. In *Haptics: Science, Technology, Applications, Proceedings of the 12th International Conference, EuroHaptics 2020, Leiden, The Netherlands, 6–9 September 2020*; Springer International Publishing: Cham, Switzerland, 2020; pp. 506–517.
29. Mahfoud, S.; Derouich, A.; Iqbal, A.; El Ouanjli, N. ANT-colony optimization-direct torque control for a doubly fed induction motor: An experimental validation. *Energy Rep.* **2022**, *8*, 81–98. [[CrossRef](#)]
30. Kim, S.J.; Kim, J.W.; Park, B.G.; Lee, D.H. A Novel Predictive Direct Torque Control Using an Optimized PWM Approach. *IEEE Trans. Ind. Appl.* **2021**, *57*, 2537–2546. [[CrossRef](#)]
31. Farah, N.; Talib, M.H.N.; Shah, N.S.M.; Abdullah, Q.; Ibrahim, Z.; Lazi, J.B.M.; Jidin, A. A novel self-tuning fuzzy logic controller-based induction motor drive system: An experimental approach. *IEEE Access* **2019**, *7*, 68172–68184. [[CrossRef](#)]
32. Hannan, M.A.; Ali, J.A.; Mohamed, A.; Hussain, A. Optimization techniques to enhance the performance of induction motor drives: A review. *Renew. Sustain. Energy Rev.* **2017**, *81*, 1611–1626. [[CrossRef](#)]
33. Reis, M.R.; de Araujo, W.R.H.; Gomes, V.M.; Silva, F.D.S.E.; Ganzaroli, C.A.; Gomes, F.A.; Wainer, G.A.; Calixto, W.P. Optimized techniques for driving and control of the switched reluctance motor to improve efficiency. *Control Eng. Pract.* **2019**, *90*, 1–18. [[CrossRef](#)]
34. Dhieb, Y.; Yaich, M.; Guermazi, A.; Ghariani, M. PID Controller Tuning using Ant Colony Optimization for Induction Motor. *J. Electr. Syst.* **2019**, *15*, 133–141.
35. George, M.A.; Kamat, D.V.; Kurian, C.P. Electronically tunable ACO based fuzzy FOPID controller for effective speed control of electric vehicle. *IEEE Access* **2021**, *9*, 73392–73412. [[CrossRef](#)]
36. Trzynadlowski, A. *The Field Orientation Principle in Control of Induction Motors*; Springer Science & Business Media: Berlin/Heidelberg, Germany, 1993. [[CrossRef](#)]
37. Albalawi, H.; Zaid, S.A.; Buswig, Y.M. Simulation Study of Two Torque Optimization Methods for Direct Torque-Controlled Induction Motors. *Appl. Sci.* **2019**, *9*, 5547. [[CrossRef](#)]
38. Balseiro, S.R.; Loiseau, I.; Ramonet, J. An Ant Colony algorithm hybridized with insertion heuristics for the Time Dependent Vehicle Routing Problem with Time Windows. *Comput. Oper. Res.* **2011**, *38*, 954–966. [[CrossRef](#)]
39. Ojha, V.K.; Abraham, A.; Snasel, V. ACO for Continuous Function Optimization: A Performance Analysis. In Proceedings of the 14th International Conference on Intelligent Systems Design and Applications (ISDA), Okinawa, Japan, 28–30 November 2014; pp. 145–150.
40. Han, Z.; Wang, Y.; Tian, D. Ant colony optimization for assembly sequence planning based on parameters optimization. *Front. Mech. Eng.* **2021**, *16*, 393–409. [[CrossRef](#)]
41. Okobiah, O.; Mohanty, S.P.; Kougiannos, E. Ordinary Kriging Metamodel-Assisted Ant Colony Algorithm for Fast Analog Design Optimization Archived 4 March 2016, at the Wayback Machine. In Proceedings of the 13th IEEE International Symposium on Quality Electronic Design (ISQED), Santa Clara, CA, USA, 19–21 March 2012; pp. 458–463.
42. Sarkar, M.; Ghosal, P.; Mohanty, S.P. Reversible Circuit Synthesis Using ACO and SA based Quinne-McCluskey Method Archived July 29, 2014, at the Wayback Machine. In Proceedings of the 56th IEEE International Midwest Symposium on Circuits & Systems (MWSCAS), Columbus, OH, USA, 4–7 August 2013; pp. 416–419.
43. Dorigo, M.; Maniezzo, V.; Colnari, A. Ant system: Optimization by a colony of cooperating agents. *IEEE Trans. Syst. Man Cybern. Part B* **1996**, *26*, 29–41. [[CrossRef](#)]
44. Zhao, Z.Y. Fuzzy Gain Scheduling of PID Controllers. *IEEE Trans. Syst. Man Cybern.* **1993**, *23*, 1392–1398. [[CrossRef](#)]

Disclaimer/Publisher’s Note: The statements, opinions and data contained in all publications are solely those of the individual author(s) and contributor(s) and not of MDPI and/or the editor(s). MDPI and/or the editor(s) disclaim responsibility for any injury to people or property resulting from any ideas, methods, instructions or products referred to in the content.